Chemosphere 286 (2022) 131478

Contents lists available at ScienceDirect

Chemosphere

journal homepage: www.elsevier.com/locate/chemosphere

Synthesis and characterization of MXene ($Ti_3C_2T_x$)/Iron oxide composite for ultrasensitive electrochemical detection of hydrogen peroxide

Ramila D. Nagarajan [a], Anandhakumar Sundaramurthy [b], Ashok K. Sundramoorthy [a,*]

[a] Department of Chemistry, SRM Institute of Science and Technology, Kattankulathur, 603 203, Tamil Nadu, India
[b] SRM Research Institute, SRM Institute of Science and Technology, Kattankulathur, 603 203, Tamil Nadu, India

ARTICLE INFO

Handling editor: Derek Muir

Keywords:
MXene-Fe_2O_3
Electroanalysis of H_2O_2
Nanomolar detection
Non-enzymatic sensors
Nanocomposite

ABSTRACT

Due to the widespread usage of hydrogen peroxide (H_2O_2) in various consumer and industrial products (Examples: fuel cells and antibacterial agents), it became important to accurately detect H_2O_2 concentration in environmental, medical and food samples. Herein, titanium carbide $Ti_3C_2T_x$ (MXene) was synthesized by using Ti, Al and C powders at high-temperature. Then, nanocrystalline iron oxide (α-Fe_2O_3) was obtained from a single solid-phase method. Using $Ti_3C_2T_x$ and Fe_2O_3 powders, $Ti_3C_2T_x$-Fe_2O_3 nanocomposite was prepared by ultrasonication. As-synthesized, $Ti_3C_2T_x$-Fe_2O_3 composite had been characterized by UV–Visible (UV–Vis), Fourier transform infrared spectroscopy (FT-IR), X-ray diffraction (XRD) and Raman spectroscopy. The Fe_2O_3 nanoparticles (NPs) were decorated on the surface of $Ti_3C_2T_x$ as observed by high resolution scanning electron microscopy (HR-SEM) and high resolution transmission electron microscopy (HR-TEM). The $Ti_3C_2T_x$ nanosheets were formed with the average size of 400–500 nm. HR-SEM images of α-Fe_2O_3 showed that the coral-like particles with the average length ~5 μm were obtained. The electrochemical properties of the individual ($Ti_3C_2T_x$ and α-Fe_2O_3) and composite materials ($Ti_3C_2T_x$-Fe_2O_3) were investigated by cyclic voltammetry (CV). $Ti_3C_2T_x$-Fe_2O_3 nanocomposite modified electrode had exhibited potent electro-catalytic activity for H_2O_2 reduction by reducing the overpotential about 320 mV and a linear response was recorded from 10 nM to 1 μM H_2O_2. The optimization of various parameters such as material composition ratio, amount of catalyst, effects of pH, scan rate and interference effects with other biomolecules were carried out. In addition, the kinetic parameters such as rate constant, diffusion coefficient and the active surface area of the electrodes were calculated. Moreover, the $Ti_3C_2T_x$-Fe_2O_3 composite modified electrode was used successfully to detect H_2O_2 in food and urine samples. We believe that $Ti_3C_2T_x$-Fe_2O_3 composite based materials could be used for the fabrication of non-enzymatic H_2O_2 sensors for medical diagnosis, food safety and environmental monitoring applications.

1. Introduction

Recently, there have been significant efforts on the innovation and development of high performance hybrid materials for the fabrication of various kinds of (bio-) chemical sensors such as electrochemical (Ruiyi et al., 2020), colorimetric (Liu et al., 2020), thermal (Yan et al., 2015), surface enhanced Raman spectroscopy (Gillibert et al., 2018), microfluidic (Park et al., 2017), fluorescent (Wang et al., 2018), paper (Mohanraj et al., 2020), disposable sensors (Tehrani and Bavarian, 2016) etc., For this purpose, the unusual properties of 2D layered materials (graphene and non-graphene layered materials) have been utilized for the diverse applications due to the their unique physical and chemical properties (Gogotsi and Anasori, 2019), (Chaudhari et al., 2017). Specifically, more efforts have been dedicated to synthesize various 2D layered materials with single atomic layer (for examples: silicene, germanene, phosphorene) and multiple atomic layers (examples: transition metal dichalcogenides and oxides) (Anasori et al., 2017). In recent years, MXenes ($M_{n+1}X_nT_x$), transition metal carbides and nitrides based layered materials have been reported (Naguib et al., 2011). In the MXene structure, 'M' represents a transition metal, 'X' is number of carbon or nitrogen and 'T' is the surface functional groups (such as F^-, O^-, OH^- and Cl^-) (Chaudhari et al., 2017). MXene could be obtained after the removal of an element from the MAX phase which was similar to graphene layers (Khazaei et al., 2017). As-prepared MXene showed metallic conductivity and hydrophilic nature due to the presence of surface terminal functional groups (Naguib et al., 2011). MXenes have

* Corresponding author.
E-mail address: ashokkus@srmist.edu.in (A.K. Sundramoorthy).

https://doi.org/10.1016/j.chemosphere.2021.131478
Received 17 March 2021; Received in revised form 11 June 2021; Accepted 6 July 2021
Available online 16 July 2021

been used in energy storage (Naguib et al., 2012), oxygen evolution reaction and hydrogen evolution reactions (Seh et al., 2016). Recently, Pd_{50}–Ru_{50}/MXene ($Ti_3C_2T_x$) nanocatalyst was effectively used for the hydrogenation process of carbon dioxide (CO_2) to methanol with high conversion efficiency of 78%, the total turnover number was 2932 in mild condition (Bharath et al., 2021a). The Ni/MAX/porous graphene composite was also used as adsorbent for the toxic metals (fluorine, lead and arsenic) in waste water. It was found that Ni/MAX/porous graphene composite was showed the maximum adsorption efficiency for Pb^{2+} (76 mg/g) ion in the contaminated ground water and industrial waste (Bharath et al., 2021b). Similarly, a pseudocapacitive deionization electrode was assembled using date seed-derived activated carbon as the anode and MAX phase (Ti_3AlC_2) as the cathode for the effective removal of chromium ions from the industrial effluents. The removal efficiency of Cr (vi) ion was 38.6 mg/g. The MXene/graphene oxide film was used in the water purification process. It had removed the negatively charged heavy metal ions ($HCrO^{4-}$, $AuCl^{4-}$ and $PdCl_4^{2-}$) and positively charged Ag^{+} ion (Xie et al., 2019). In addition, three dimensional MXene-graphene oxide hydrogel was effectively used in photo-catalysis (Chen et al., 2019a). For example, 2D MXene decorated with 1D cadmium sulphide was used for the photocatalytic coupling reaction of H_2 generation and selective conversion of bioethanol into 1,1-diethoxyethane (Li et al., 2020). These new studies were supported that MXene/MAX phase could be used as the catalyst for the hydrogenation, photocatalysis and desalination process (Bharath et al., 2020).

On the other hand, detection of H_2O_2 is very important in the environmental, textile, clinical, pharmaceutical and food samples (Chen et al., 2013). Because, H_2O_2 had been used as a preserving agent for milk and also used to produce cheese. Normally, the concentration of H_2O_2 in raw milk sample was 1–2 mg/mL, when the concentration was ten times higher, it destroys the pathogens (Ivanova et al., 2019). However, if the excess H_2O_2 present in the milk which may degrade the nutritional compounds (folic acid) which is essential for the human body (Silva et al., 2012). The common beverages (green tea, black tea and instant coffee) contains more than 100 μM H_2O_2. If the H_2O_2 directly enters into our gastrointestinal tract and it can cause the digestion related problems. The levels of H_2O_2 concentration can be easily detected by analysing a freshly voided human urine (Halliwell et al., 2000). Apart from these, H_2O_2 is also formed as a by-product of enzyme catalysed reactions (for example: glucose oxidase reaction, lactate and cholesterol oxidase reactions). In the biological reaction, H_2O_2 was used as a mediator for measuring the level of product conversion of glucose, lactose and cholesterol (Shamkhalichenar and Choi, 2020). The elevated level of H_2O_2 could cause carcinogenesis and became the vital indicator of cancer and heart attack in humans (Maji et al., 2014). For a normal person, the intracellular concentration of H_2O_2 should be less than 10 nM, and in plasma, the H_2O_2 concentration might be 100–5000 times greater than the intracellular H_2O_2 levels (Forman et al., 2016). Generally, conventional methods such as titrimetric (V Klassen et al., 1994), fluorescence (Yu et al., 2019) and colorimetric (Teodoro et al., 2019) methods had been used for the detection of H_2O_2. However, these methods had shown low sensitivity and also oxidize the other compounds present in the sample and lead to poor accuracy (Gimeno et al., 2013). So, analysis of H_2O_2 in plasma sample is became very challenging.

In a recent study, horse radish peroxidase (HRP) was immobilized on MXene and used it for the detection of H_2O_2 from 5 to 1650 μM and the limit of detection (LOD) was 0.74 μM (Bao-Kai et al., 2019). MXene/-haemoglobin (Hb) based biosensor was also reported for the detection of H_2O_2 due to the enhanced bio-electrocatalytic activity of heme (Wang et al., 2015a). However, these enzyme based electrodes had shown some drawbacks such as tedious electrode preparation, instability of the enzymes under various temperatures, pre-treatment requirements (He et al., 2014), need of perm-selective ion-exchange membrane (Nafion) (Lv et al., 2016), glutaraldehyde cross-linker (Akyilmaz et al., 2017) and bovine serum albumin (Tripathi et al., 2006) for the successful immobilization process. To avoid these problems, Lorencova et al. reported MXene ($Ti_3C_2T_x$) based electrochemical sensor for the analysis of H_2O_2. They had also investigated the effectiveness of $Ti_3C_2T_x$ as an electro-catalyst for H_2O_2 before and after oxidation of MXene ($oTi_3C_2T_x$). They found that pristine $Ti_3C_2T_x$ showed better electro-catalytic performance than the oxidized $Ti_3C_2T_x$ for the analysis of H_2O_2 at −0.5 V (Lorencova et al., 2017). Also, to further enhance the electrocatalytic activity and reduce the over potential, nanocomposite of MXene/platinum nanoparticles ($Ti_3C_2T_x$-Pt NPs) was also prepared. The electro-reduction of H_2O_2 was observed at 0.25 V on $Ti_3C_2T_x$-Pt NPs modified glassy carbon electrode (GCE) and the linear response was observed from 490 μM to 53.6 mM with the LOD of 448 nM. Similarly, $Ti_3C_2T_x$-Pt/Nafion (Nf) modified GCE was also used for the detection of small biomolecules (Dopamine, ascorbic acid, uric acid and acetaminophen) (Lorencova et al., 2018). MXene-Pt/polyaniline sensor was also developed for the determination of H_2O_2 (from 1 μM to 7 mM) and lactic acid (from 0.005 to 5 mM) (Neampet et al., 2019). In these methods, precious and expensive metal (Pt) catalysts were used and also these sensors had shown poor stability.

In this work, for the first time, $Ti_3C_2T_x$-Fe_2O_3 nanocomposite was prepared and used to detect H_2O_2 in nanomolar levels. The MAX phase was prepared by ball-milling of titanium, aluminium and graphite powders for 12 h. Then the obtained product was heated at 1100 °C for 2 h and followed by HF etching resulted in the formation of $Ti_3C_2T_x$. For the α-Fe_2O_3 preparation, a single step synthesis method was developed by using β-cyclodextrin (β-CD; supramolecule), urea and iron acetate as precursors. Finally, $Ti_3C_2T_x$-Fe_2O_3 nanocomposite was obtained by mixing MXene and Fe_2O_3 (10:1) via ultra-probe sonicator and used to modify the electrode surface. $Ti_3C_2T_x$-Fe_2O_3 modified electrode was showed an enhanced electro-catalytic activity for H_2O_2 reduction due to synergistic effects between $Ti_3C_2T_x$ and α-Fe_2O_3. For comparison, H_2O_2 reduction was also carried out with the $Ti_3C_2T_x$, α-Fe_2O_3 and $Ti_3C_2T_x$-Fe_2O_3. It was found that the composite ($Ti_3C_2T_x$-Fe_2O_3) modified electrode showed high stability, electro-catalytic activity, wide linear range of detection (from 10 nM to 1 μM H_2O_2) and lower limit of detection (LOD) (7.46 nM). Furthermore, the nanocomposite modified electrode was used for the analysis of H_2O_2 in milk and urine samples with high selectivity.

2. Experimental

2.1. Materials and methods

Iron acetate [$Fe(CH_3COO)_2$], β-cyclodextrin (β-CD) and dopamine hydrochloride (DA) were purchased from Sigma-Aldrich (USA). H_2O_2, ascorbic acid (AA), uric acid (UA), para-acetaminophen (PA), oxalic acid (OA), glucose, lactose, monosodium hydrogen phosphate (NaH_2PO_4) and disodium hydrogen phosphate (Na_2HPO_4) were obtained from SRL, India. The phosphate buffer solution (PBS) (0.1 M) was prepared using NaH_2PO_4 and Na_2HPO_4 (pH = 7.2) for the sensing of H_2O_2. All the experiments were performed with the milli-Q-water (18.2 MΩ cm @ 25 ± 2 °C).

The electronic transitions of the catalyst $Ti_3C_2T_x$-Fe_2O_3 and α-Fe_2O_3 were studied by using the UV–Visible spectrophotometer (UV 3600 plus, Shimadzu). The functional groups of the materials were analysed by attenuated total reflection (ATR) - FT-IR spectrophotometer (Shimadzu, IRTracer 100). The composite formation was confirmed by X-ray diffraction spectrometer (XRD-PAN analytical XpertPro), Netherlands. The Raman spectrum of $Ti_3C_2T_x$-Fe_2O_3 and $Ti_3C_2T_x$ were recorded using a Micro Raman spectrometer-Labram HR evolution (Horiba, Japan). The surface morphologies of the samples were analysed with the HR-SEM and the elemental compositions were identified by using Energy dispersive X-ray spectroscopy (EDX-FEI Quanta 200). The selected area electron diffraction (SAED) pattern and the surface morphology of the $Ti_3C_2T_x$-Fe_2O_3 composite were recorded by HR-TEM, 2100 plus Electron microscope (JEOL, Japan). The electrochemical activities of $Ti_3C_2T_x$-

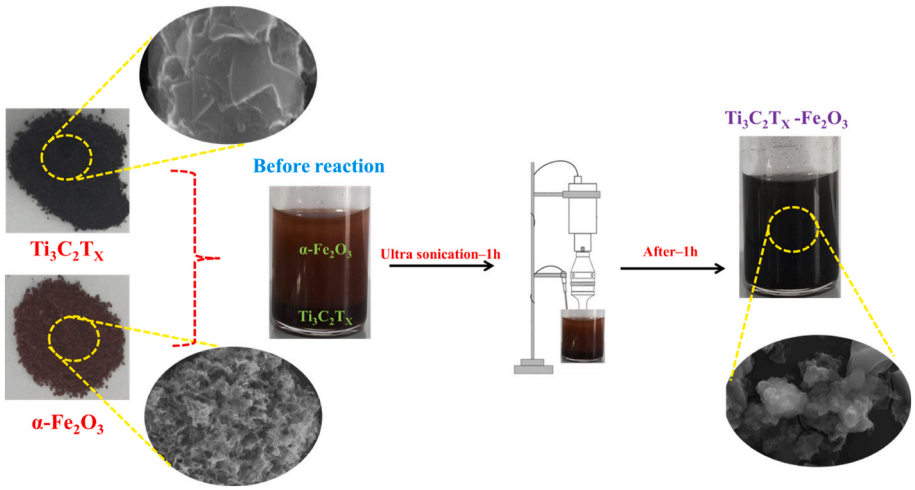

Fig. 1. The schematic representation for the preparation of $Ti_3C_2T_x$-Fe_2O_3 composite (10:1) by using $Ti_3C_2T_x$ and α-Fe_2O_3 powders.

Fe_2O_3, $Ti_3C_2T_x$ and α-Fe_2O_3 were investigated by using a three electrode system with an electrochemical workstation (CH Instruments Model: CHI-760 E, USA). All the experiments were carried out at the room temperature (25 ± 2 °C).

2.2. Synthesis of α-Fe_2O_3

The solid phase synthesis of α-Fe_2O_3 was carried out by using the precursors of $Fe(CH_3COO)_2$, β-CD and urea. $Fe(CH_3COO)_2$ (0.125 g) was grinded well with the β-CD (0.5 g) and urea (0.5 g) by pestle and mortar. The weight ratio of the compounds was 1:4:4. After grinding, a pale orange colour powder was obtained and the mixture was transferred to a quartz boat and annealed at the temperature of 300 °C in a tubular furnace (the temperature increment was 5 °C/min). The sample was kept at 300 °C for 6 h under air. After that, the heating was stopped and furnace temperature was decreased to the room temperature. The final product of α-Fe_2O_3 (red brick powder) was obtained and used for the characterization and sensing application of H_2O_2. The α-Fe_2O_3 dispersion was prepared by dissolving 10 mg of α-Fe_2O_3 in 20 mL 1:1 ethanol: water mixture with 20 μL Nafion (5%) followed by probe-sonication for 1 h at controlled temperature with ice-bath.

2.3. Preparation of $Ti_3C_2T_x$-Fe_2O_3 composite

The $Ti_3C_2T_x$ powder was synthesized as reported elsewhere (Murugan et al., 2021). $Ti_3C_2T_x$ powder (100 mg) and α-Fe_2O_3 (10 mg) were mixed by ultrasonication in 1:1 ethanol:water mixture (20 mL) to obtain $Ti_3C_2T_x$-Fe_2O_3 co-dispersion (Fig. 1). To find out the best composition ratio of the materials for the electro-analysis of H_2O_2, $Ti_3C_2T_x$-α-Fe_2O_3 containing dispersions were prepared with different weight ratios ($Ti_3C_2T_x$-Fe_2O_3; 10:1, 1:1 and 1:10 ratio) in 1:1 ethanol:water mixture (20 mL). In order to obtain a homogenous dispersion, $Ti_3C_2T_x$ and α-Fe_2O_3 powders were ultra-sonicated for 60 min with 55% amplitude for 3 s ON and 2 s OFF. The visual images of 1:10, 1:1 and10:1 ratio nanocomposite dispersions were shown in Fig. S1. Similarly, (100 mg) $Ti_3C_2T_x$ and (10 mg) α-Fe_2O_3 dispersions were also individually prepared for control experiments.

2.4. Electrode preparation

For the analysis of H_2O_2, the $Ti_3C_2T_x$-Fe_2O_3 modified GCE (φ = 3 mm) and rotating disk electrode (RDE) (φ = 5 mm) were prepared. Prior to the modification, the GCE was polished with alumina slurry (0.05 μm) on a polishing cloth until the mirror like surface appeared. After GCE was cleaned, the $Ti_3C_2T_x$-Fe_2O_3 dispersion (6 μL) was drop casted on the electrode surface and dried in hot air oven at 50 °C for 5 min. The control experiments were carried out separately with $Ti_3C_2T_x$ and α-Fe_2O_3 modified electrodes. Before the electrochemical measurements, the 0.1 M PBS was purged with nitrogen gas for 10 min to remove the dissolved oxygen. The oxygen reduction reaction (ORR) was carried out in different electrolytes (0.1 M H_2SO_4, 0.1 M NaOH and 0.1 M PBS).

2.5. Detecting H_2O_2 in real samples

Three kinds of milk samples were analysed: (i) concentrated milk sample, (ii) the diluted milk sample with PBS, and (iii) milk extract obtained after centrifugation at 15000 rpm which removed the milk proteins/fats (Hira et al., 2020). For the (i) concentrated milk sample analysis: milk sample (50 μL) was taken without any dilution and added into the 0.1 M PBS. Followed by, the known concentrations of H_2O_2 were added into the 0.1 M PBS and the recovery percentages were calculated (Li et al., 2014). (ii) For the diluted milk sample analysis: 50 μL milk sample was diluted with 0.1 M PBS (50 mL) containing 10 μM H_2O_2. The diluted milk sample with H_2O_2 was analysed and the recovery percentage was calculated (Li et al., 2018). (iii) For the milk extract analysis; the collected supernatant milk extract was added in to the electrolyte solution and sensing of H_2O_2 was carried out before and after the standard additions of H_2O_2 and recovery percentages were calculated. H_2O_2 analysis in urine sample was carried out as follows: urine sample was collected from a normal person and the sample (100 μL) was diluted with 50 mL PBS and spiked with 10 μM H_2O_2. After that, H_2O_2 in the diluted sample was detected and the recovery percentage was calculated (Palanisamy et al., 2015).

3. Results and discussion

3.1. UV–vis, FT-IR, XRD and Raman characterizations

UV–visible absorption (UV–vis) spectrum of α-Fe_2O_3 was showed three absorption peaks (Fig. S2A, curve i). The first transition band observed around 322 nm corresponds to the charge transfer from ligand to metal (LMCT). The another transition observed at 543 nm for the double excitons process from $^6A_1$ (^6s)+$^6A_1$ (^6s) to $^4T_1$ ($_4G$)+$^4T_1$ (^4G), it was the overlapped contribution of $^6A_1$ (^6s) to ^4E, $^4A_1$ (^4G) which was related to the ligand transition at 433 nm and the charge transfer tail (Mallick and Dash, 2013). The inter-band transition at 543 nm was responsible for the red brick powder of α-Fe_2O_3. The above mentioned absorption bands were clearly indicated the formation of α-Fe_2O_3 (Rufus et al., 2016). However, for the $Ti_3C_2T_x$-Fe_2O_3 composite sample, the electronic transitions bands of α-Fe_2O_3 were red shifted due to the

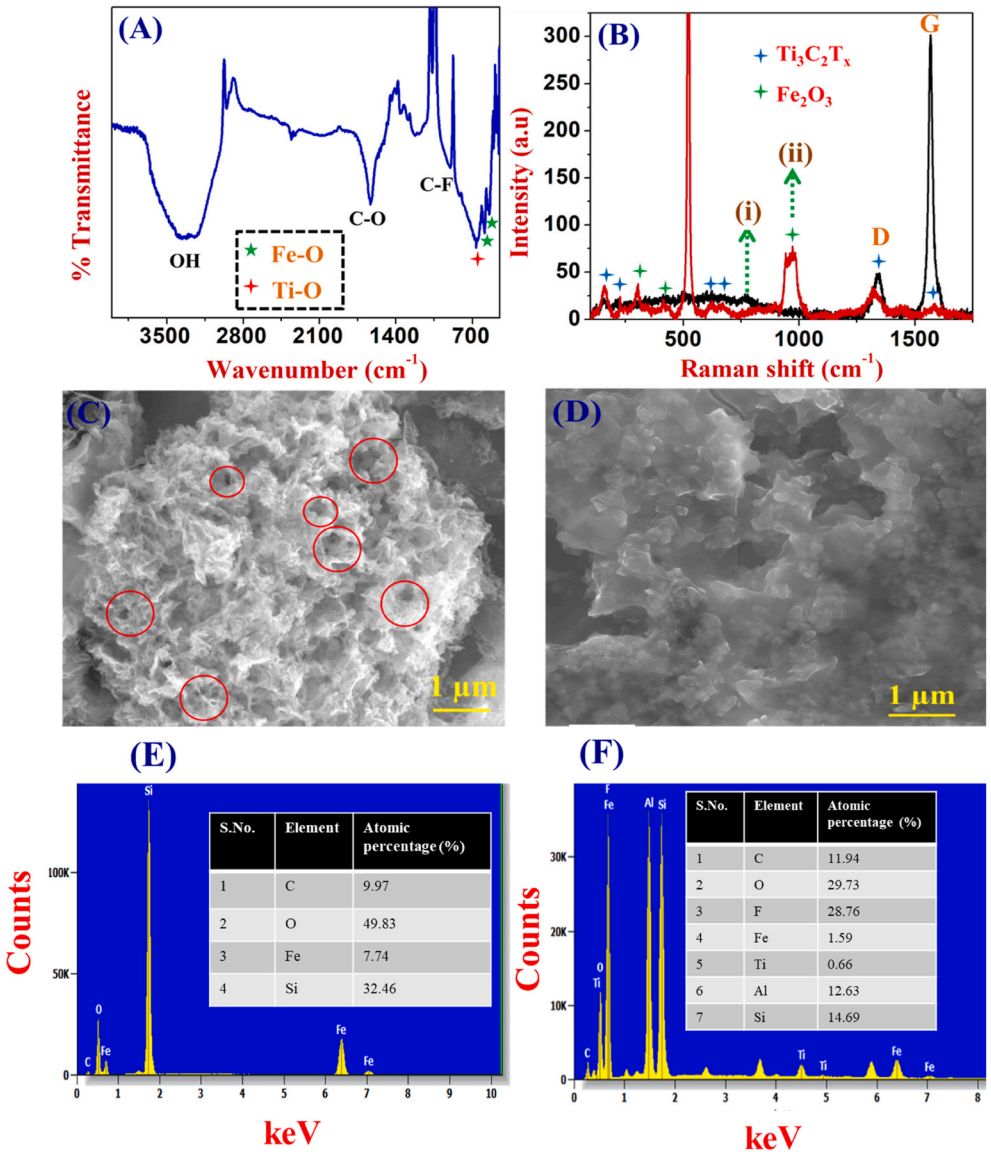

Fig. 2. (A) FT-IR spectrum of $Ti_3C_2T_x$-Fe_2O_3 composite. (B) Raman spectrum (using 532 laser excitation) of (i) $Ti_3C_2T_x$ and (ii) $Ti_3C_2T_x$-Fe_2O_3 composite. (C and D) HR-SEM images and (E and F) EDX spectrum of α-Fe_2O_3 (C & E) and $Ti_3C_2T_x$-Fe_2O_3 (D & F) samples.

interaction between $Ti_3C_2T_x$ and α-Fe_2O_3 (Uma et al., 2020). These results were in agreement with the earlier reports of Ti_3C_2–Fe_2O_3 composite (Zhang et al., 2018).

FT-IR spectra of α-Fe_2O_3, $Ti_3C_2T_x$ and $Ti_3C_2T_x$-Fe_2O_3 samples were recorded. Fig. S2B shows multiple IR bands at 3174 (O–H stretching), 1417 (O–H bending), 1523 (C–O stretching) and 1067 cm^{-1} (C–F vibration) which revealed the presence of various functional groups such as –OH, C–O, and C–F on $Ti_3C_2T_x$ surface. The IR band at 667 cm^{-1} was indicated the deformation of Ti–O bond (Chen et al., 2019b; Dong et al., 2019). For the α-Fe_2O_3 sample, Fe–O (metal oxide) vibration bands observed at 545 and 590 cm^{-1} (Fig. S2C). Next, the IR spectrum of the $Ti_3C_2T_x$-Fe_2O_3 composite was recorded (Fig. 2A), which showed the IR peaks responsible for the both $Ti_3C_2T_x$ and Fe_2O_3. The new IR bands were appeared at 540 and 584 cm^{-1} correspond to the Fe–O (metal--oxygen) vibrations (Rufus et al., 2016). In addition, IR bands observed for the composite were down shifted to (17 cm^{-1}) 652 cm^{-1} (Ti–O), (5 cm^{-1}) 540 cm^{-1} and 584 cm^{-1} (Fe–O), which may be due to the synergetic effect between the negatively charged $Ti_3C_2T_x$ and the positively charged α-Fe_2O_3. From the FT-IR spectra, the presence of surface functional groups on $Ti_3C_2T_x$ and the metal-oxygen vibration of $Ti_3C_2T_x$-Fe_2O_3 composite were confirmed (Zou et al., 2018). Fig. S3 displays the XRD spectra of α-Fe_2O_3, $Ti_3C_2T_x$, and $Ti_3C_2T_x$-Fe_2O_3 composite materials. The $Ti_3C_2T_x$ (Fig. S3, curve-ii) was showed the major diffraction peaks appeared at 36.02, 41.9 and 60.88° correspond for the TiC (111), (200) and (220) planes. These planes were matched with the standard values of $TiC_{0.67}$ [JCPDS No 00-032-1383]. Some additional oxide peaks of Ti and Al were also appeared. The diffraction peaks of TiO_2 were observed at 25.2, 37.7, 48.1, 54.9° and the Al_2O_3 peaks were appeared at 52.7 and 57.2°. The presence of both Al_2O_3 and TiO_2 peaks were indicated the formation of mixed phase MXene (Parse et al., 2019). Next, the α-Fe_2O_3 formation was also confirmed by XRD. Fig. S3 (curve i) showed major diffraction peaks appeared at 33 and 35.5° correspond to the (104) and (110) plane of α-Fe_2O_3 (Townsend et al., 2011). The other XRD peaks of α-Fe_2O_3 were located at 24.17, 40.8, 49.58, 53.8, 57.65, 62.6, 63.8 and 71.78°. These observed XRD peaks confirmed the formation α-Fe_2O_3 rather than the other forms of iron oxides and iron hydroxides which matched with the JCPDS card no (89–8103) (Townsend et al., 2011). Finally, the XRD spectrum of the $Ti_3C_2T_x$-Fe_2O_3 composite was recorded (Fig. S3, curves iii). The $Ti_3C_2T_x$-Fe_2O_3 was showed the presence of both diffraction peaks of TiO_2 and the Fe_2O_3.

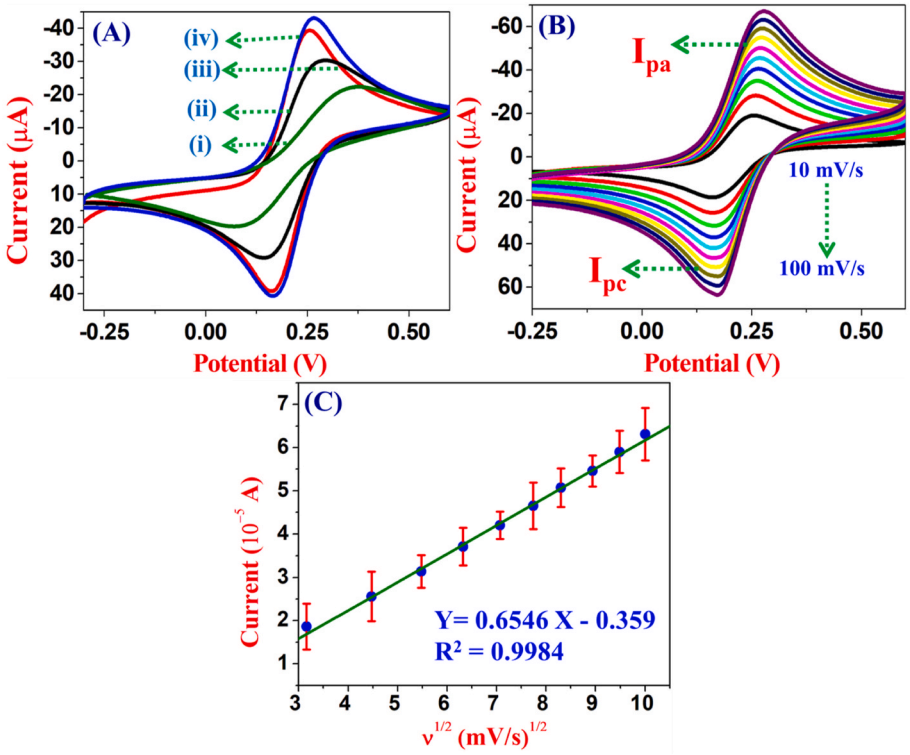

Fig. 3. (A) CVs were recorded in 0.1 M KCl containing 5 mM $[Fe(CN)_6]^{3-/4-}$ using (i) α-Fe_2O_3, (ii) $Ti_3C_2T_x$, (iii) bare-GCE, and (iv) $Ti_3C_2T_x$-Fe_2O_3 modified GCE at a scan rate of 50 mV/s (B) CVs were recorded with different scan rates from 10 to 100 mV/s in 0.1 M KCl containing 5 mM $[Fe(CN)_6]^{3-/4-}$ using $Ti_3C_2T_x$-Fe_2O_3 modified GCE. (C) The linear plot was made between the square root of scan rates and I_{pc} (each measurement was taken three times and the mean values were given, N = 3).

The XRD peaks at 25.2 and 37.7° correspond to the TiO_2 vibrations and 57.5° for the Al_2O_3 peak. The other major diffraction peaks were observed at 24.3, 33.16, 35.68, 49.8, 54 and 64° correspond to the Fe_2O_3. These XRD peaks of TiO_2 and the Fe_2O_3 were confirmed the formation of $Ti_3C_2T_x$-Fe_2O_3 composite (Li et al., 2019).

Fig. 2B represents the Raman spectra of $Ti_3C_2T_x$ and $Ti_3C_2T_x$-Fe_2O_3 composite. The different vibration bands of (Ti–C, Ti–Al and Fe–O) $Ti_3C_2T_x$ and composite were recorded using 532 nm laser excitation. The Raman band located at 157 cm^{-1} was due to the vibrational mode of anatase phase of TiO_2. For the $Ti_3C_2T_x$, the major Raman bands were observed at 215 (Ti–Al vibrations), 352 (vibration atoms in $Ti_3C_2T_x$), 620 and 688 cm^{-1} (Ti–C bond vibrations) (Cao et al., 2017), which confirmed the existence of $Ti_3C_2T_x$ (Melchior et al., 2018). Graphitic carbon peaks were also appeared at 1342 (D band due to defects in carbon material) and 1569 cm^{-1} (G band corresponds to the sp^2 hybridized carbon vibration) of 2D hexagonal lattice (Parse et al., 2019). In the case of $Ti_3C_2T_x$-Fe_2O_3 composite, the Fe–O vibrational peaks were appeared at 304, 412 and 827 cm^{-1} (Testa-Anta et al., 2019). Furthermore, D band (at 1326 cm^{-1}) and the G band (1583 cm^{-1}) were down shifted compared to $Ti_3C_2T_x$ (alone). In addition, the D band intensity was increased for the composite and the G band position was upshifted to higher wavenumber (1569–1583 cm^{-1}). The calculated I_D/I_G ratio was 2.3 which indicated the less defects on the composite surface compared to the pristine $Ti_3C_2T_x$. The reason for the G band shift on $Ti_3C_2T_x$-Fe_2O_3 composite might be due to the isolated presence of double bonds (Dubale et al., 2014).

3.2. Surface morphology analysis

The thin-films of $Ti_3C_2T_x$, α-Fe_2O_3 and $Ti_3C_2T_x$-Fe_2O_3 were prepared on silica substrates and the surface morphologies were analysed by HR-SEM. As-synthesized $Ti_3C_2T_x$ nanosheets were showed few sheets like structures (Fig. S4A-B). It clearly indicated that sheets-like morphology with the average sizes of 400–500 nm were present. The thickness of the $Ti_3C_2T_x$ film was ~180 nm and the lateral spacing was about 0.354 nm. Next, synthesized α-Fe_2O_3 was showed the coral-like microstructure which was helpful to enhance the catalytic activity (Fig. 2C) (Wang et al., 2015b). From the HR-SEM images of $Ti_3C_2T_x$-Fe_2O_3, it was found that Fe_2O_3 nanoparticles (NPs) were strongly attached on the $Ti_3C_2T_x$ sheets and the NPs sizes were found to be ~100 nm (Fig. 2D) (Zou et al., 2018). As indicated, the MXene sheets were decorated with Fe_2O_3 NPs during ultasonication process. The EDX analysis was also performed on α-Fe_2O_3 and $Ti_3C_2T_x$-Fe_2O_3 composite samples. $Ti_3C_2T_x$ was showed the presence of Ti, Al, fluorine, oxygen and carbon. Interestingly, in addition to the above elements, Fe was present in the composite (Fig. 2E and F). These elemental analysis were again confirmed that $Ti_3C_2T_x$-Fe_2O_3 composite was successfully formed. Furthermore, $Ti_3C_2T_x$-Fe_2O_3 nanocomposite was also investigated by the HR-TEM. The surface morphology image of the nanocomposite showed that the Fe_2O_3 particles were decorated on the surface of the $Ti_3C_2T_x$ sheets (Fig. S5A). The $Ti_3C_2T_x$ sheets were strongly attached with Fe_2O_3 nanoparticles and enhanced the catalytic activity of Fe_2O_3 by synergistic effect (Zou et al., 2018). The selected area electron diffraction (SAED) pattern of the composite was recorded which indicated that a polycrystalline structure was obtained (Fig. S5B). The set of concentric rings were indexed to the major planes (104), (116) and (214). Those planes were corresponded to the diffraction patterns of α-Fe_2O_3 (Li et al., 2019). These planes and the d-spacing values were matched with the XRD analysis. This further corroborated that the α-Fe_2O_3 nanoparticles were decorated on the surface of the $Ti_3C_2T_x$ sheet by electrostatic attraction.

3.3. Kinetic studies of $Ti_3C_2T_x$ and $Ti_3C_2T_x$-Fe_2O_3 modified electrodes

In order to understand the electron transfer behaviour and calculate the surface areas of the modified electrodes, cyclic voltammograms (CVs) were recorded in 0.1 M KCl containing 5 mM K_2 $[Fe(CN)_6]$/K_3 $[Fe(CN)_6]$ using bare GCE (curve-iii) and modified GCEs with α-Fe_2O_3 (curve i), $Ti_3C_2T_x$ (curve-ii) and $Ti_3C_2T_x$-Fe_2O_3 (curve-iv) films which

Table 1
CVs were recorded in 0.1 M KCl containing 5 mM K_2 $[Fe(CN)_6]/K_3$ $[Fe(CN)_6]$ using different modified electrodes and their electrode potentials and the current values were compared.

S. No.	Types of electrodes	E_{pa} (V)	E_{pc} (V)	$E^{o'}$ (V)	ΔE_p (mV)	I_{pa} (μA)	I_{pc} (μA)
1	bare-GCE	0.256	0.162	0.21	94	−39.66	39.13
2	$Ti_3C_2T_X$/GCE	0.287	0.15	0.22	137	−30.21	29.022
3	Fe_2O_3/GCE	0.367	0.08	0.224	287	−22.2	19.35
4	$Ti_3C_2T_x$-Fe_2O_3/GCE	0.26	0.17	0.215	90	−43.19	40.19

showed the well-defined redox peaks (Fig. 3A). The calculated formal potential's ($E^{o'}$), peak to peak separation (ΔE_p) and redox peak currents of $[Fe(CN)_6]^{3-/4-}$ were listed in Table 1. The lowest peak separation and higher redox peak (I_{pa} and I_{pc}) currents were observed for $Ti_3C_2T_x$-Fe_2O_3 composite modified GCE compared to bare-GCE, $Ti_3C_2T_x$/GCE, Fe_2O_3/GCE (Table 1). For the $Ti_3C_2T_x$ modified electrode, the ΔE_p was about 137 mV due to the surface functional groups of F^-, OH^- and O^- which are negatively charged (Lorencova et al., 2020). The density of free electrons on $Ti_3C_2T_x$ and the surface functional groups were the reasons for higher peak separation (Nayak et al., 2018). The higher electro-catalytic activity of $Ti_3C_2T_x$-Fe_2O_3 modified electrode might have resulted from the synergistic effect between positively charged α-Fe_2O_3 and negatively charged MXene (Zou et al., 2018) (Fig. 3A). Compared to the individual materials, $Ti_3C_2T_x$-Fe_2O_3 modified GCE had showed high current enhancement about 10%.

CVs were also recorded using $Ti_3C_2T_x$-Fe_2O_3/GCE at different scan rates from 10 to 100 mV/s (Fig. 3B). A linear plot was established between the square roots of scan rate *vs*. the cathodic peak currents (I_{pc}), the linear curve was obtained with the regression coefficient (R^2) of 0.9984 (Fig. 3C). Next, the active surface area of $Ti_3C_2T_x$-Fe_2O_3/GCE was calculated using the Randles-Sevcik equation (1)(Bard et al., 1980)

$$I_{pa} = \left(2.69 \times 10^5\right) n^{3/2} D^{1/2} C_O \nu^{1/2} A \quad (1)$$

where, 'n' is number of electrons (n = 1), C is the concentration of $[Fe(CN)_6]^{3-/4-}$ (5 mM), D is the diffusion coefficient (7.6×10^{-6} cm^2/s) and A is surface area of the electrode. Using the above equation, the electrochemically active surface area of each modified electrodes were calculated. The active surface areas of bare GCE, $Ti_3C_2T_x$/GCE and $Ti_3C_2T_x$-Fe_2O_3/GCE were found to be 0.113, 0.10 and 0.18 cm^2, respectively. Due to the electrostatic attraction between $Ti_3C_2T_x$ and α-Fe_2O_3, the composite modified electrode was showed higher surface active area. The surface roughness factor (R_f) was calculated using the equation $R_f = A_{real}/A_{Geo}$ (real surface area/geometric surface area) as 0.18/0.07 = 2.5 (Tavakkoli et al., 2020), which indicated the enhanced surface area of the composite modified GCE.

3.4. Electrochemical properties of $Ti_3C_2T_x$ and $Ti_3C_2T_x$-Fe_2O_3

After modification of GCE with 6 μL of $Ti_3C_2T_x$ or $Ti_3C_2T_x$-Fe_2O_3 dispersion by drop casting method and the electrode was dried at 50 °C for 5 min. After that, the modified electrode was washed with distilled water to remove any unbounded materials from the surface. Fig. 4A shows CVs recorded using bare GCE (curve-i), $Ti_3C_2T_x$/GCE (curve-ii) and $Ti_3C_2T_x$-Fe_2O_3/GCE (curve-iii). Interestingly, α-Fe_2O_3 incorporated $Ti_3C_2T_x$ film had exhibited redox peak of Fe^{2+}/Fe^{3+} at −0.195 V, and $Ti_3C_2T_x$ redox peak was centred at −0.45 V in 0.1 M PBS (curve-iii). Normally, the formal redox potential ($E^{o'}$) of Fe^{2+}/Fe^{3+} should be 0.4 V (Amreen and Senthil Kumar, 2018). If the iron present in the heme protein, the formal potential was located at −0.34 V (Zheng et al., 2008). Similarly, after incorporation of α-Fe_2O_3 in to $Ti_3C_2T_x$, the $E^{o'}$ of Fe was found at −0.195 V which was negatively shifted about 595 mV compared to the normal redox potential of Fe^{2+}/Fe^{3+} (0.4 V). The $E^{o'}$ for the redox peak of α-Fe_2O_3 was found at 0.15 V, however, the redox peak of Fe was negatively shifted about +250 mV for $Ti_3C_2T_x$-Fe_2O_3/GCE (Amreen and Senthil Kumar, 2018). The presence of both redox peaks of $Ti_3C_2T_x$ and α-Fe_2O_3 were demonstrated that the composite had higher catalytic activity compared to $Ti_3C_2T_x$ and α-Fe_2O_3. The redox peak of the $Ti_3C_2T_x$ was observed at ($E^{o'}$) −0.45 V vs. Ag/AgCl. This redox peak was assigned to the intercalation of H^+ cations from the electrolyte solution (electrosorption) and pseudocapacitance behaviour of $Ti_3C_2T_x$ at

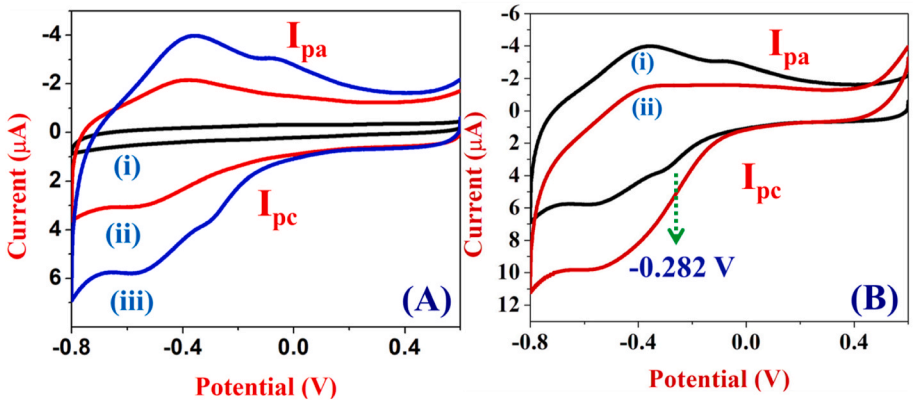

Fig. 4. (A) CVs of different modified electrodes were recorded in 0.1 M PBS using (i) bare-GCE, (ii) $Ti_3C_2T_x$/GCE and (iii) $Ti_3C_2T_x$-Fe_2O_3/GCE. (B) CVs were recorded by using $Ti_3C_2T_x$-Fe_2O_3/GCE in the (i) absence and (ii) presence of 400 nM H_2O_2 at the scan rate of 50 mV/s.

Table 2
CVs were recorded using different modified electrodes in 0.1 M PBS and their electrode potentials and current values were compared.

S. No.	Types of electrode	E_{pa} (V)	E_{pc} (V)	$E^{o'}$ (V)	ΔE_p (mV)	I_{pa} (μA)	I_{pc} (μA)
1	Bare-GCE	–	–	–	–	–	–
2	$Ti_3C_2T_x$/GCE	−0.38	−0.516	−0.45	136	−2.19	2.93
3	α-Fe_2O_3/GCE	0	−0.3	0.15	300	−0.3	0.32
4	$Ti_3C_2T_x$-Fe_2O_3/GCE	Fe_2O_3 (−0.10) and $Ti_3C_2T_x$(-0.368)	Fe_2O_3 (-0.29) and $Ti_3C_2T_x$(-0.54)	Fe_2O_3 (-0.195) and $Ti_3C_2T_x$ (-0.454)	Fe_2O_3 (190) and $Ti_3C_2T_x$ (172)	Fe_2O_3 (−3.63) and $Ti_3C_2T_x$(-3.52)	Fe_2O_3 (3.34) and $Ti_3C_2T_x$ (4.70)

Table 3
The analysis of 400 nM H_2O_2 was carried out using different modified electrodes in 0.1 M PBS and their reduction potentials were compared.

S. No.	Types of electrode	Onset reduction potential of H_2O_2 (V)
1	Bare-GCE	−0.6
2	$Ti_3C_2T_X$/GCE	−0.585
3	Fe_2O_3/GCE	−0.3
4	$Ti_3C_2T_x$-Fe_2O_3/GCE (10:1)	−0.28
5	$Ti_3C_2T_x$-Fe_2O_3/GCE different composition ratios (1:10) and (1:1)	−0.6

the surface. The intercalation/deintercalation of $Ti_3C_2T_x$ exhibited that reversible redox peak (Yang et al., 2018). The ratio of the obtained anodic and cathodic peak currents values were nearly unity which indicated the highly reversible nature of the redox peak. The calculated redox potential's and the corresponding peak currents were shown in Table 2.

3.5. Electroanalysis of H_2O_2 on $Ti_3C_2T_x$-Fe_2O_3/GCE

To test the electro-catalytic activity against H_2O_2, the different modified electrodes were prepared (*see Experimental section 2.4*). The electro-reduction of 400 nM H_2O_2 was tested on bare, $Ti_3C_2T_x$ and $Ti_3C_2T_x$-Fe_2O_3 modified GCEs. The $Ti_3C_2T_x$-Fe_2O_3/GCE was showed H_2O_2 reduction at −0.282 V (Fig. 4B, curve ii). H_2O_2 was reduced on bare GCE at around −0.60 V (Fig. S6A), it was found that after modification with $Ti_3C_2T_x$ (Fig. S6B), H_2O_2 reduction peak was enhanced and observed at −0.585 V due to the presence of functional groups on the surface (Lorencova et al., 2017). We also modified the electrode with α-Fe_2O_3 which showed H_2O_2 reduction at −0.3 V (Fig. S7A). Table 3 illustrates the onset potential for the reduction of H_2O_2 on different modified electrodes. From the obtained results, $Ti_3C_2T_x$-Fe_2O_3/GCE had showed high sensitivity and catalytic current for H_2O_2 reduction at lower potential which may be due to the synergetic effect between α-Fe_2O_3 and $Ti_3C_2T_x$. The synergetic effect might have come from the strong interaction between α-Fe_2O_3 and $Ti_3C_2T_x$ which acted as an electrocatalyst for the reduction process. We had also prepared $Ti_3C_2T_x$-Fe_2O_3 film with the different compositions ratios of (1:1 and 1:10) and used them for the reduction of H_2O_2. The H_2O_2 reduction peaks were appeared at −0.6 V (Fig. S7B and C). The composites prepared with 1:1 and 1:10 ($Ti_3C_2T_x$:Fe_2O_3) ratio had shown poor stability due to the excessive presence of α-Fe_2O_3 and the less active sites on $Ti_3C_2T_x$ for functionalization.

3.6. Effect of catalyst loading

To optimize the suitable catalyst loading for electro-reduction of H_2O_2, the different volume of $Ti_3C_2T_x$-Fe_2O_3 (10:1) dispersion was used to modify GCE's for the electrochemical analysis. The amounts of catalyst loading were varied from 10 to 50 μg of $Ti_3C_2T_x$-Fe_2O_3 (by increasing the volumes) on the GCE surface from the stock concentration of 5 mg/mL (Karthik et al., 2018). Each modified electrodes were used to record CVs in 0.1 M PBS in the absence and presence of 400 nM H_2O_2. Fig. S8A shows the CVs of various $Ti_3C_2T_x$-Fe_2O_3 modified electrodes with different amount of catalyst loaded in 0.1 M PBS containing 400 nM H_2O_2. The catalytic currents were increased with the amount of catalyst. This experiment was also repeated three times. As shown in Fig. S8B, a non-linear plot was prepared between the catalyst loadings and I_{pc} of H_2O_2. As shown in Fig. S8B, when the amount of catalyst was increased from (10–50 μg), the reduction current was also increased and started to decrease after (30 μg) reaching the maximum catalyst loading. The possible reason may be due to the poor diffusion of H_2O_2 in to the electrode surface because of the dense film formation, so 50 μg of catalyst resulted the catalytic current of 0.54 μA (Wang et al., 2019). From this study, (30 μg) was selected as the optimum amount of electrocatalyst for the reduction of H_2O_2 (the net reduction current was 1.36 μA at the potential 0.282 V). The 30 μg of $Ti_3C_2T_x$-Fe_2O_3 (10:1)

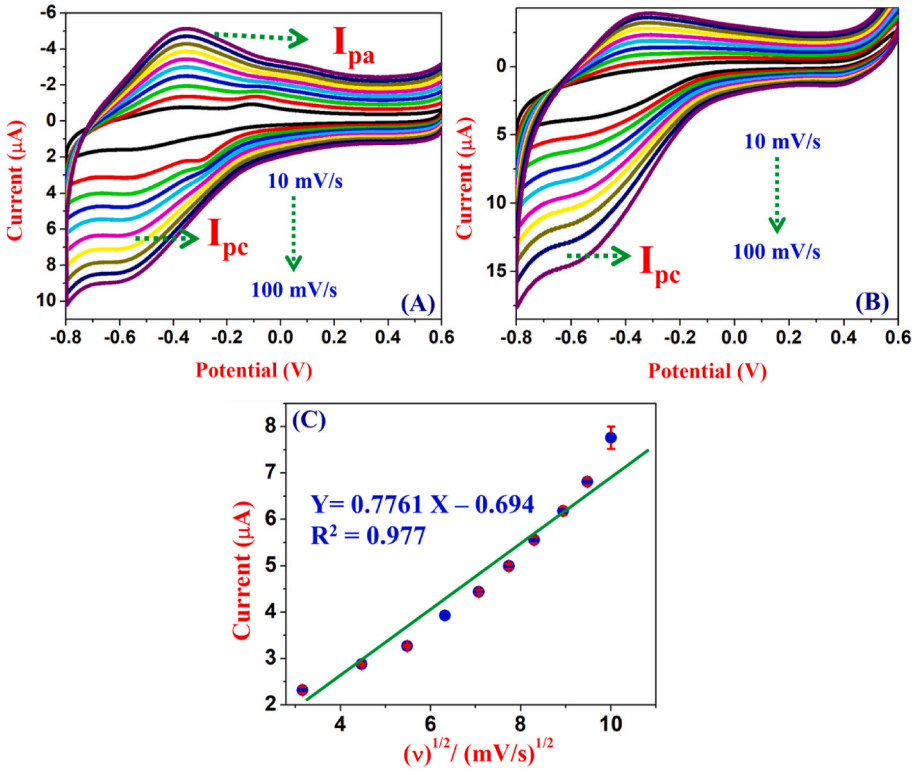

Fig. 5. (A) CVs of $Ti_3C_2T_x$-Fe_2O_3/GCE @ different scan rates from 10 to 100 mV/s in 0.1 M PBS. (B) CVs of $Ti_3C_2T_x$-Fe_2O_3/GCE @ different scan rates from 10 to 100 mV/s in 0.1 M PBS containing 400 nM H_2O_2. (C) The linear plot was made between square root of scan rates and reduction currents of H_2O_2.

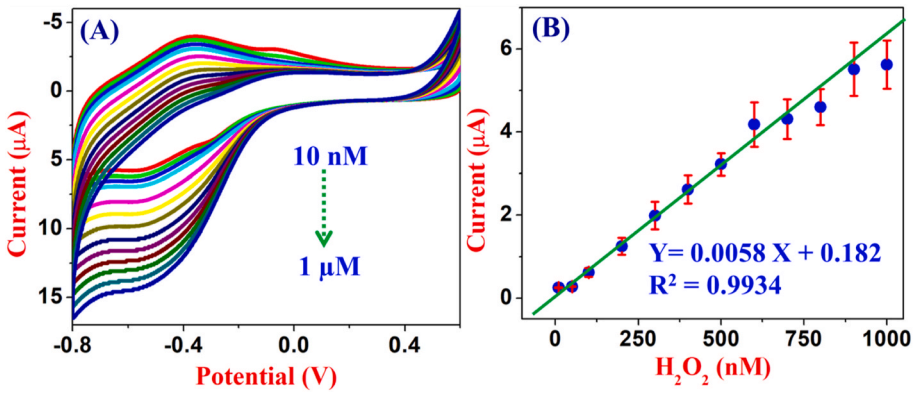

Fig. 6. (A) CVs were recorded in PBS with different concentrations of H_2O_2 from 10 nM–1 μM at a scan rate of 50 mV/s. (B) The calibration plot was made between the concentration of H_2O_2 and net reduction current of H_2O_2 (This experiment was repeated three times, N = 3).

dispersion was used to modify the GCE for further electrochemical experiments.

3.7. Effect of pH

The influence of pH on the electro-catalytic activity of $Ti_3C_2T_x$-Fe_2O_3/GCE was studied by CV. The redox peak of Fe was found to be pH dependent and the redox potential was positively shifted with the increase of pH from 4 to 8. Fig. S9A shows that the cathodic peak potential was systematically shifted with the pH of the solution. The relationship between the pH and the cathodic peak potential was 35 mV/pH, which was nearly equal to 30 mV/pH, indicated the non-Nernstian response (transfer of unequal number of protons/electrons) of the electrode process (Amreen and Senthil Kumar, 2018). The effect of pH on H_2O_2 decomposition could be explained; H_2O_2 was more stable in acidic pH and started to decompose above pH 6. It was found that when the pH of the buffer solution was increased from 4 to 8, the reduction current response for the 400 nM H_2O_2 was also increased (Torres et al., 2014; Jung et al., 2009). The obtained net current value for H_2O_2 reduction at the $Ti_3C_2T_x$-Fe_2O_3 (in pH~7.2) was 1.47 μA (Fig. S9B) which was higher than other pH. From this study, pH 7.2 was found to be the optimum pH for electro-analysis of H_2O_2. The electro-catalytic reduction of H_2O_2 can be explained on $Ti_3C_2T_x$-Fe_2O_3 by using the following equations (2) and (3) (Zhang et al., 2010; Liu et al., 2013)

$$Ti_3C_2T_x - Fe^{(III)} + e^- \rightarrow Ti_3C_2T_x - Fe^{(II)} \quad (2)$$

$$Ti_3C_2T_x - Fe^{(II)} + 2H_2O_2 \rightarrow Ti_3C_2T_x - Fe^{(III)} + 2H_2O + O_2 \quad (3)$$

3.8. Effect of scan rate

CVs were recorded using $Ti_3C_2T_x$-Fe_2O_3 modified electrode at different scan rates from 10 to 100 mV/s (Fig. 5A). The anodic (I_{pa}) and cathodic peak (I_{pc}) currents were increased linearly with the increasing of scan rates. The linear relationship between logarithmic of scan rate *vs.* (E_{pa}) and (E_{pc}) resulted with the slope values of 66 mV dec^{-1} and 74 mV dec^{-1}. The electron transfer coefficient (α) and electron transfer rate constant (k_s) were calculated using the Laviron equation. The anodic and cathodic charge transfer coefficient values were obtained using the following equation and (Bard et al., 1980). The average electron transfer coefficient (α) was estimated as 0.6 which indicated that $Ti_3C_2T_x$-Fe_2O_3 modified electrode favours the H_2O_2 reduction reaction. Based on the above parameters, the heterogeneous rate constant (k_s) was calculated by using the following equation (4) (Li et al., 2015)

$$\log k_s = \alpha \log(1-\alpha) + (1-\alpha)log - \log\left(\frac{RT}{nF\nu}\right) - \frac{\alpha(1-\alpha)nF\Delta Ep}{2.3RT} \quad (4)$$

The calculated k_s value was 0.04 s^{-1} which was comparatively smaller than the reported values. It indicated that the electron transfer reaction was relatively sluggish (Bard et al., 1980). Fig. 5B shows CVs recorded for the electro-reduction of 400 nM H_2O_2 on $Ti_3C_2T_x$-Fe_2O_3/GCE at different scan rates. It showed that cathodic peak current increases linearly with the square root of scan rate (Fig. 5C) and the correlation coefficient (R^2) value was 0.977. The linear plot of log ν *vs.* I_{pc} gave a slope value of 0.519 (Y = 0.519 X – 0.207). It was close to the theoretical value of 0.5 for a diffusion controlled electrochemical reduction process of H_2O_2 (Amreen and Kumar, 2018).

3.9. Electro-catalytic reduction of H_2O_2 on $Ti_3C_2T_x$-Fe_2O_3

Fig. 6A shows CVs of $Ti_3C_2T_x$-Fe_2O_3/GCE in 0.1 M PBS with the increasing concentration of H_2O_2 from 10 to 1000 nM at a scan rate of 50 mV/s. The electro-reduction peak of H_2O_2 on $Ti_3C_2T_x$-Fe_2O_3/GCE showed the linear range of signals from 10 to 1000 nM H_2O_2 (Amreen and Kumar, 2018). The H_2O_2 reduction peak current (I_{pc}) *vs.* H_2O_2 concentration established a linear calibration plot (Fig. 6B) with the slope value of Y = 0.0058 X + 0.182. The LOD was calculated to be 7.46 nM using the following equation: LOD = 3.3 × standard deviation of the blank/slope of the calibration curve (Olsen, 1986). The sensitivity of the $Ti_3C_2T_x$-Fe_2O_3 modified electrode for the analysis of H_2O_2 was 0.32 μA/nM cm^2. The LOD of our proposed method was comparable with the myoglobin immobilized on manganese doped molybdenum diselenide electrode (Ramaraj et al., 2019). For comparison, the performance of α-Fe_2O_3 modified electrode was also tested, it showed a linear range of detection from 5 to 30 μM (Fig. S10). It was confirmed that $Ti_3C_2T_x$-Fe_2O_3 modified electrode was more promising than α-Fe_2O_3 modified electrode.

Linear sweep voltammetry (LSV) measurements were also carried out using the $Ti_3C_2T_x$-Fe_2O_3/GCE for detection of H_2O_2 in the range from 100 to 1000 nM. Fig.S11 shows voltammograms of changes in reduction peak currents vs. H_2O_2 concentrations at the onset potential of −0.28 V. The LSV was also confirmed that a linear response of the electrode was observed up to 1000 nM H_2O_2. Using LSVs, a Tafel plot was drawn from the saturation point of current-voltage curves which was related to the rate determining step. The linear plot of log (current) *vs.* potential (E) gave a slope value of 293 mV dec^{-1}. The rate determining step was calculated using equation (5) (Amreen and Senthil Kumar, 2018).

$$b_c = 2.303\, RT/n\alpha F \quad (5)$$

Finally, the charge transfer coefficient (α) was obtained from the cathodic Tafel plot slope, α value was found to be 0.7, which favoured the reduction process (Bard et al., 1980).

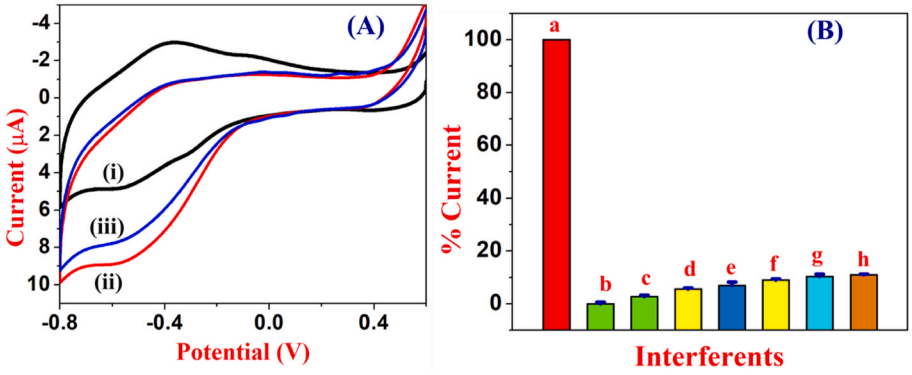

Fig. 7. (A) The CVs of $Ti_3C_2T_x$-Fe_2O_3/GCE were tested in 0.1 M PBS with interfering biomolecules: (i) 0 nM H_2O_2, (ii) 500 nM H_2O_2, and (iii) 500 nM H_2O_2 plus 100 μM of each interfering molecules (AA, UA, OA, PA, glucose, lactose and DA) at a scan rate of 50 mV/s. (B) The bar diagram represents the current percentages calculated from the CV curves from the analysis of (a) H_2O_2 with interfering molecules, (b) AA, (c) UA, (d) OA, (e) PA, (f) glucose, (g) lactose and (h) DA. This experiment was repeated three times and the mean values were provided.

3.9.1. Chronoamperometry

The stability and electrochemical activity of the $Ti_3C_2T_x$-Fe_2O_3 catalyst was examined by using chronoamperometry (CA). Chronoamperograms were recorded in the potential window of 0.8 to −0.6 V in de-aerated 0.1 M PBS under the constant stirring at 400 rpm with different H_2O_2 concentrations. For this experiment, RDE – 5 mm (0.2 cm^2) was modified with 6 μL of $Ti_3C_2T_x$-Fe_2O_3. Fig. S12A shows the current responses recorded with the time in the absence and presence of H_2O_2 by standard addition method from 0.1 to 1 μM. The chronoamperogram curves were showed the steady state approximation for the each addition of H_2O_2 within ~3.3 s (response). This value was higher than (t > 1.5 s), so it was indicated that electro-reduction rate of H_2O_2 was lower than the rate of H_2O_2 diffusion (Majidi et al., 2015). A linear plot was established between the 'I' vs. $t^{-1/2}$ which gave a straight line. The diffusion coefficient 'D' value was calculated using the Cottrell equation (6).

$$I = nFAD^{1/2}C/\sqrt{\pi t} \quad (6)$$

The obtained slope values was used for the calculation of diffusion coefficient of H_2O_2. To calculate the 'D' value, the slope of each line was plotted to obtain the average D value of 7.37×10^{-4} cm^2/s (Fig. S12B) (Majidi et al., 2015) (Fatahi et al., 2017). Next, a calibration plot was established between the concentrations of H_2O_2 vs. the reduction current from chronoamperometry (Fig. S12C). The linear regression equation was obtained as $Y = 1.36 \times 10^{-7} + 8.87 \times 10^{-5}$ and the R^2 value was 0.9954.

3.9.2. Selectivity of $Ti_3C_2T_x$ -Fe_2O_3 modified electrode

Selectivity is the most important aspects of sensor. The Selectivity of $Ti_3C_2T_x$-Fe_2O_3 electrode towards H_2O_2 was verified in the presence of various biochemicals by using CV. The selectivity of $Ti_3C_2T_x$-Fe_2O_3 was studied under optimized condition with the different biomolecules (interferences) such as 100 μM of AA, UA, PA, OA, glucose, lactose and DA which were added in to the solution in the presence of 500 nM H_2O_2 (Fig. 7A). Interestingly, there were no changes observed in the H_2O_2 reduction potential at −0.28 V upon addition of the above mentioned biochemicals. From this study, the tolerance limit was obtained as 200 times greater than the concentration of each interfering molecules that makes the error percentage around ±10% with the 500 nM H_2O_2 (Fig. 7B). This result was indicated that the effect of interfering compounds was negligible. The mechanism for the high selectivity was due to the selective reduction of H_2O_2 by Fe, which was not possible with the other interfering molecules (DA, AA, UA, OA, PA and glucose). The reduction of H_2O_2 was followed the transfer of electron to the Fe^{3+} ion and converted to H_2O. This electron transfer process was unfavourable with the electrochemical oxidation process of these studied biomolecules. For instance, the DA gets oxidized at +0.2 V which may not interfere at negative potential. This study confirmed that H_2O_2 was selectively reduced on $Ti_3C_2T_x$-Fe_2O_3 modified electrode.

3.9.3. Oxygen reduction reaction (ORR)

The $Ti_3C_2T_x$-Fe_2O_3/GCE was studied in the cathodic potential window and suitable for the reduction of oxygen and hydrogen peroxide. We had already explained about the $Ti_3C_2T_x$-Fe_2O_3 modified electrode towards the reduction of H_2O_2 in PBS. To test the efficiency of the $Ti_3C_2T_x$-Fe_2O_3 modified electrode for ORR applications, CVs were recorded using the $Ti_3C_2T_x$-Fe_2O_3/GCE in O_2 and N_2 saturated electrolyte solutions (0.1 M H_2SO_4, 0.1 M NaOH and 0.1 M PBS). In 0.1 M H_2SO_4, the $Ti_3C_2T_x$-Fe_2O_3 showed an oxygen reduction peak at −0.335 V with the current of 3.89 μA (Fig. S13A, curve iii), in the case of 0.1 M NaOH, reduction peak was at −0.420 V (Fig. S13B). In 0.1 M PBS, ORR was observed at -0.6 V with the peak current of 3.76 μA (Fig. S13C). When we compared with the previous reports, MXene based electrodes were showed ORR at -590 and -500 mV in acidic and alkali environments (Lorencova et al., 2017). As shown in our study, when Fe_2O_3 was incorporated with MXene, the reduction potential was further reduced about 255 mV compared to the pristine $Ti_3C_2T_x$ in acidic electrolyte. It was due to the presence of Fe_2O_3 which helped to enhance the electrocatalytic reaction towards the reduction of O_2. It was confirmed that $Ti_3C_2T_x$-Fe_2O_3 acted as a good electro-catalyst for the ORR in both alkaline and acidic environments.

Using the double potential-step technique, the coulometric behaviours of $Ti_3C_2T_x$-Fe_2O_3/GCE and bare electrode were analysed in the presence and absence of oxygen. Using $Ti_3C_2T_x$-Fe_2O_3/GCE, chronocoulometry curves were recorded in O_2 and N_2 saturated solutions. The $Ti_3C_2T_x$-Fe_2O_3/GCE was showed more couloumetric charge than the bare GCE in oxygen saturated electrolyte (Fig. S14). It confirmed that the $Ti_3C_2T_x$-Fe_2O_3 had shown more capacitive charge behaviour than the unmodified electrode with enhanced electro-catalytic activities towards H_2O_2 and oxygen reduction.

3.9.4. Repeatability, reproducibility and long-term stability of the sensor

For the sensing applications, the repeatability, reproducibility and stability of the sensors are more important factors. To check the reproducibility of the sensor, the $Ti_3C_2T_x$-Fe_2O_3 modified electrodes were independently prepared for ten times and their RSD value was obtained as 0.079% for blank measurements and 0.4% for the analysis of H_2O_2. The repeatability of the sensor was tested by repeating the analysis of 400 nM H_2O_2 @ $Ti_3C_2T_x$-Fe_2O_3 electrode after different storage periods of 0, 24, 48 and 72 h. The sensors were retained their responses about 93.8%. Next, the stability of $Ti_3C_2T_x$-Fe_2O_3/GCE was tested by recording continuous CVs for 50 cycles in 0.1 M PBS, the electrode response was decreased only about 13%. This showed that the $Ti_3C_2T_x$-Fe_2O_3/GCE had exhibited good stability after repeated analysis and storage time (Fig. S15A). The long-term stability of the $Ti_3C_2T_x$-Fe_2O_3 modified RDE was tested by analysing 400 nM H_2O_2 at constant rotating speed of 500 rpm up to 2000 s in 0.1 M PBS. In this study, 200 and 400 nM H_2O_2 were spiked at the time interval of 50 s, the stability of the electrode was calculated. It showed that the sensor retained 79% of its efficiency after the whole experiments (Fig. S15B).

Table 4
Analysis of H_2O_2 in milk and urine samples using $Ti_3C_2T_x$-Fe_2O_3 modified electrode. This experiment was repeated three times and the RSD values were provided.

S. No.	Real samples	Added (nM)	Found (nM)	Recovery (%)	RSD (%)
1.	Centrifuged milk samples	100	97.7	97.7	1.744
		200	196.8	98.4	1.522
		300	293.2	97.7	2.37
2	Diluted milk sample	100	96.4	96.4	1.85
		200	195.4	97.7	2.488
		300	294.5	98.16	1.93
3	Concentrated milk sample	100	93.8	93.8	1.22
		200	192.1	96.05	1.414
		300	288.8	96.26	2.56
4	Urine sample	100	96.9	96.9	0.57
		200	194.2	97.1	1.13
		300	291.7	97.2	1.56

The procedure for the real sample analysis was described in the experimental section. The practical applications of the sensor was tested by detecting H_2O_2 in milk and urine samples. The CVs were recorded with the milk samples using $Ti_3C_2T_x$-Fe_2O_3 modified electrode. Fig.S16 represents the CVs recorded for the $Ti_3C_2T_x$-Fe_2O_3 modified electrode in the absence (curve-i) and presence of 50 μL concentrated milk sample (curve-ii) in 0.1 M PBS. Using CV, H_2O_2 concentration in various milk samples were analysed after spiking various known concentrations of H_2O_2 from 100 to 300 nM. The recovery percentages of H_2O_2 were obtained from 94 to 97%. These results clearly indicated that $Ti_3C_2T_x$-Fe_2O_3 modified electrode may be used for the analysis of H_2O_2 in real samples with satisfactory results. The same experiment was repeated three more times to calculate the RSD and the recovery percentages as shown in Table 4.

4. Conclusions

For the first time, the $Ti_3C_2T_x$-Fe_2O_3 modified electrode had been reported for electro-catalytic reduction of H_2O_2 and oxygen. It was demonstrated that $Ti_3C_2T_x$-Fe_2O_3 can be used as an effective electro-catalyst instead of the noble metals (Pt, Au and Ag) and the enzyme based sensors reported for the electro-reduction of H_2O_2 and O_2. The $Ti_3C_2T_x$, α-Fe_2O_3 and the $Ti_3C_2T_x$-Fe_2O_3 nanocomposite had been comprehensively characterized by using Raman, XRD, FT-IR, UV–Vis, HR-SEM, EDX and HR-TEM. From the overall characterization and analysis of $Ti_3C_2T_x$-Fe_2O_3, it was found that the electrostatic interactions and surface functional groups of $Ti_3C_2T_x$ helped for strong adherence of Fe_2O_3 NPs. The selective applications of $Ti_3C_2T_x$-Fe_2O_3 modified electrode towards the electro-reduction of H_2O_2 was demonstrated by using CV, CA and LSV techniques. The important kinetic parameters such as effective surface area, D value, α, and the rate constant (k_s) were calculated for the $Ti_3C_2T_x$-Fe_2O_3 modified electrode. For the reduction of H_2O_2, the optimization studies were carried out. The analytical data of the modified electrode showed that $Ti_3C_2T_x$-Fe_2O_3 can be used for the detection of H_2O_2 from 10 to 1000 nM with the LOD of 7.46 nM. The $Ti_3C_2T_x$-Fe_2O_3 modified electrode was also exhibited a long term stability as it confirmed by RDE. The $Ti_3C_2T_x$-Fe_2O_3 sensor was also showed good reproducibility for continuous usage for up to 72 h. The $Ti_3C_2T_x$-Fe_2O_3 modified electrode was finally applied for the practical application in the detection of H_2O_2 in food and biological samples with acceptable accuracy.

Credit author statement

Ramila Nagarajan: Conceptualization, Methodology, Experimental, Analysis, Writing- Original draft preparation. Anandhakumar Sundaramurthy: Methodology, Data analysis, Editing. Ashok Sundramoorthy: Supervision, Writing- Reviewing and Editing.

Declaration of competing interest

The authors declare that they have no known competing financial interests or personal relationships that could have appeared to influence the work reported in this paper.

Acknowledgements

We would like to acknowledge the Department of Science and Technology (DST) and Science and Engineering Research Board (SERB), Government of India for financial support through Early Career Research Award (Ref. No.: ECR/2016/001446). We also thank the Department of Science and Technology (International Bilateral Cooperation Division) for financial support through “INDO-RUSSIA Project (INT/RUS/RFBR/385)”. NR acknowledges CSIR -SRF fellowship from Council of Scientific and Industrial Research (CSIR), Government of India. Award no-09/1045(0043)/2020-EMR-I.

Appendix A. Supplementary data

Supplementary data to this article can be found online at https://doi.org/10.1016/j.chemosphere.2021.131478.

References

Akyilmaz, E., Oyman, G., Cınar, E., Odabas, G., 2017. A new polyaniline–catalase–glutaraldehyde-modified biosensor for hydrogen peroxide detection. Prep. Biochem. Biotechnol. 47, 86–93.
Amreen, K., Kumar, A.S., 2018. A human whole blood chemically modified electrode for the hydrogen peroxide reduction and sensing: real-time interaction studies of hemoglobin in the red blood cell with hydrogen peroxide. J. Electroanal. Chem. 815, 189–197.
Amreen, K., Senthil Kumar, A., 2018. Highly redox-active hematin-functionalized carbon mesoporous nanomaterial for electrocatalytic reduction applications in neutral media. ACS Appl. Nano Mater. 1, 2272–2283.
Anasori, B., Lukatskaya, M.R., Gogotsi, Y., 2017. 2D metal carbides and nitrides (MXenes) for energy storage. Nat. Rev. Mater. 2, 1–17.
Bao-Kai, M.A., Li, M., Cheong, L.-Z., Xin-Chu, W., Shen, C., Huang, Q., 2019. Enzyme-MXene nanosheets: fabrication and application in electrochemical detection of H2O2. J. Inorg. Mater. 35 (1), 131–138.
Bard, A.J., Faulkner, L.R., Leddy, J., Zoski, C.G., 1980. Electrochemical Methods: Fundamentals and Applications. wiley, New York.
Bharath, G., Hai, A., Rambabu, K., Savariraj, D., Ibrahim, Y., Banat, F., 2020. The fabrication of activated carbon and metal-carbide 2D framework-based asymmetric electrodes for the capacitive deionization of Cr(vi) ions toward industrial wastewater remediation. Environ. Sci. Water Res. Technol. 6, 351–361.
Bharath, G., Rambabu, K., Hai, A., Othman, I., Ponpandian, N., Banat, F., Loke Show, P., 2021a. Hybrid Pd50-Ru50/MXene (Ti3C2Tx) nanocatalyst for effective hydrogenation of CO2 to methanol toward climate change control. Chem. Eng. J. 414, 128869.
Bharath, G., Hai, A., Rambabu, K., Pazhanivel, T., Hasan, S.W., Banat, F., 2021b. Designed assembly of Ni/MAX (Ti3AlC2) and porous graphene-based asymmetric electrodes for capacitive deionization of multivalent ions. Chemosphere 266, 129048.
Cao, Y., Deng, Q., Liu, Z., Shen, D., Wang, T., Huang, Q., Du, S., Jiang, N., Lin, C.-T., Yu, J., 2017. Enhanced thermal properties of poly (vinylidene fluoride) composites with ultrathin nanosheets of MXene. RSC Adv. 7, 20494–20501.
Chaudhari, N.K., Jin, H., Kim, B., San Baek, D., Joo, S.H., Lee, K., 2017. MXene: an emerging two-dimensional material for future energy conversion and storage applications. J. Mater. Chem. A. 5, 24564–24579.
Chen, S., Yuan, R., Chai, Y., Hu, F., 2013. Electrochemical sensing of hydrogen peroxide using metal nanoparticles: a review. Microchim. Acta. 180, 15–32.
Chen, Y., Xie, X., Xin, X., Tang, Z.-R., Xu, Y.-J., 2019a. Ti3C2Tx-Based three-dimensional hydrogel by a graphene oxide-assisted self-convergence process for enhanced photoredox catalysis. ACS Nano 13, 295–304.
Chen, J., Yuan, X., Lyu, F., Zhong, Q., Hu, H., Pan, Q., Zhang, Q., 2019b. Integrating MXene nanosheets with cobalt-tipped carbon nanotubes for an efficient oxygen reduction reaction. J. Mater. Chem. A. 7, 1281–1286.
Dong, Y., Sang, D., He, C., Sheng, X., Lei, L., 2019. Mxene/alginate composites for lead and copper ion removal from aqueous solutions. RSC Adv. 9, 29015–29022.
Dubale, A.A., Su, W.-N., Tamirat, A.G., Pan, C.-J., Aragaw, B.A., Chen, H.-M., Chen, C.-H., Hwang, B.-J., 2014. The synergetic effect of graphene on Cu 2 O nanowire arrays as a highly efficient hydrogen evolution photocathode in water splitting. J. Mater. Chem. A. 2, 18383–18397.
Fatahi, A., Malakooti, R., Shahlaei, M., 2017. Electrocatalytic oxidation and determination of dexamethasone at an Fe 3 O 4/PANI–Cu II microsphere modified carbon ionic liquid electrode. RSC Adv. 7, 11322–11330.

Forman, H.J., Bernardo, A., Davies, K.J.A., 2016. What is the concentration of hydrogen peroxide in blood and plasma? Arch. Biochem. Biophys. 603, 48–53.
Gillibert, R., Triba, M.N., Lamy de la Chapelle, M., 2018. Surface enhanced Raman scattering sensor for highly sensitive and selective detection of ochratoxin A. Analyst 143, 339–345.
Gimeno, M.P., Mayoral, M.C., Andres, J.M., 2013. A potentiometric titration for H 2 O 2 determination in the presence of organic compounds. Anal. Methods. 5, 1510–1514.
Gogotsi, Y., Anasori, B., 2019. The rise of MXenes. ACS Nano 13, 8491–8494.
Halliwell, B., Clement, M.V., Long, L.H., 2000. Hydrogen peroxide in the human body. FEBS Lett. 486, 10–13.
He, S., Zhang, B., Liu, M., Chen, W., 2014. Non-enzymatic hydrogen peroxide electrochemical sensor based on a three-dimensional MnO2 nanosheets/carbon foam composite. RSC Adv. 4, 49315–49323.
Hira, S.A., Muthuchamy, N., Rajendran, K., Song, S., Park, S., Lee, J.-M., Joo, S.H., Park, K.H., 2020. Ultrasensitive detection of hydrogen peroxide and dopamine using copolymer-grafted metal-organic framework based electrochemical sensor. Anal. Chim. Acta 1118, 26–35.
Ivanova, A.S., Merkuleva, A.D., V Andreev, S., Sakharov, K.A., 2019. Method for determination of hydrogen peroxide in adulterated milk using high performance liquid chromatography. Food Chem. 283, 431–436.
Jung, Y.S., Lim, W.T., Park, J., Kim, Y., 2009. Effect of pH on fenton and fenton-like oxidation. Environ. Technol. 30, 183–190.
Karthik, R., Kumar, J.V., Chen, S.-M., Sundaresan, P., Mutharani, B., Chen, Y.C., Muthuraj, V., 2018. Simple sonochemical synthesis of novel grass-like vanadium disulfide: a viable non-enzymatic electrochemical sensor for the detection of hydrogen peroxide. Ultrason. Sonochem. 48, 473–481.
Khazaei, M., Ranjbar, A., Arai, M., Sasaki, T., Yunoki, S., 2017. Electronic properties and applications of MXenes: a theoretical review. J. Mater. Chem. C. 5, 2488–2503.
Li, D., Luo, L., Pang, Z., Chen, X., Cai, Y., Wei, Q., 2014. Amperometric detection of hydrogen peroxide using a nanofibrous membrane sputtered with silver. RSC Adv. 4, 3857–3863.
Li, M., Dong, S., Li, N., Tang, H., Zheng, J., 2015. Magnetic Fe 3 O 4 carbon aerogel and ionic liquid composite films as an electrochemical interface for accelerated electrochemistry of glucose oxidase and myoglobin. RSC Adv. 5, 14704–14711.
Li, J., Jiang, J., Xu, Z., Liu, M., Tang, S., Yang, C., Qian, D., 2018. Facile synthesis of Ag@Cu2O heterogeneous nanocrystals decorated N-doped reduced graphene oxide with enhanced electrocatalytic activity for ultrasensitive detection of H2O2. Sensor. Actuator. B Chem. 260, 529–540.
Li, F., Liu, Y.-L., Wang, G.-G., Zhang, H.-Y., Zhang, B., Li, G.-Z., Wu, Z.-P., Dang, L.-Y., Han, J.-C., 2019. Few-layered Ti3C2Tx MXenes coupled with Fe2O3 nanorod arrays grown on carbon cloth as anodes for flexible asymmetric supercapacitors. J. Mater. Chem. A. 7, 22631–22641.
Li, J.-Y., Li, Y.-H., Zhang, F., Tang, Z.-R., Xu, Y.-J., 2020. Visible-light-driven integrated organic synthesis and hydrogen evolution over 1D/2D CdS-Ti3C2Tx MXene composites. Appl. Catal. B Environ. 269, 118783.
Liu, X., Liu, J., Chang, Z., Luo, L., Lei, X., Sun, X., 2013. α-Fe2O3 nanorod arrays for bioanalytical applications: nitrite and hydrogen peroxide detection. RSC Adv. 3, 8489–8494.
Liu, B., Zhuang, J., Wei, G., 2020. Recent advances in the design of colorimetric sensors for environmental monitoring. Environ. Sci. Nano. 7, 2195–2213.
Lorencova, L., Bertok, T., Dosekova, E., Holazova, A., Paprckova, D., Vikartovska, A., Sasinkova, V., Filip, J., Kasak, P., Jerigova, M., Velic, D., Mahmoud, K.A., Tkac, J., 2017. Electrochemical performance of Ti(3)C(2)T(x) MXene in aqueous media: towards ultrasensitive H2O2 sensing. Electrochim. Acta 235, 471–479.
Lorencova, L., Bertok, T., Filip, J., Jerigova, M., Velic, D., Kasak, P., Mahmoud, K.A., Tkac, J., 2018. Highly stable Ti3C2Tx (MXene)/Pt nanoparticles-modified glassy carbon electrode for H2O2 and small molecules sensing applications. Sensor. Actuator. B Chem. 263, 360–368.
Lorencova, L., Gajdosova, V., Hroncekova, S., Bertok, T., Jerigova, M., Velic, D., Sobolciak, P., Krupa, I., Kasak, P., Tkac, J., 2020. Electrochemical investigation of interfacial properties of Ti3C2Tx MXene modified by aryldiazonium betaine derivatives. Front. Chem. 8, 553.
Lv, Y., Wang, F., Zhu, H., Zou, X., Tao, C., Wang, J., 2016. Electrochemically reduced graphene oxide-nafion/Au nanoparticle modified electrode for hydrogen peroxide sensing. Nanomater. Nanotechnol. 6, 30.
Maji, S.K., Sreejith, S., Mandal, A.K., Ma, X., Zhao, Y., 2014. Immobilizing gold nanoparticles in mesoporous silica covered reduced graphene oxide: a hybrid material for cancer cell detection through hydrogen peroxide sensing. ACS Appl. Mater. Interfaces 6, 13648–13656.
Majidi, M.R., Pournaghi-Azar, M.H., Saadatirad, A., Alipour, E., 2015. Simple and rapid amperometric monitoring of hydrogen peroxide at hemoglobin-modified pencil lead electrode as a novel biosensor: application to the analysis of honey sample. Food Anal. Methods. 8, 1067–1077.
Mallick, P., Dash, B.N., 2013. X-ray diffraction and UV-visible characterizations of#-Fe 2 O 3 nanoparticles annealed at different temperature. Nanosci. Nanotechnol. 3, 130–134.
Melchior, S.A., Raju, K., Ike, I.S., Erasmus, R.M., Kabongo, G., Sigalas, I., Iyuke, S.E., Ozoemena, K.I., 2018. High-voltage symmetric supercapacitor based on 2d titanium carbide (mxene, ti2ctx)/carbon nanosphere composites in a neutral aqueous electrolyte. J. Electrochem. Soc. 165, A501.
Mohanraj, J., Durgalakshmi, D., Rakkesh, R.A., Balakumar, S., Rajendran, S., Karimi-Maleh, H., 2020. Facile synthesis of paper based graphene electrodes for point of care devices: a double stranded DNA (dsDNA) biosensor. J. Colloid Interface Sci. 566, 463–472.
Murugan, N., Jerome, R., Preethika, M., Sundaramurthy, A., Sundramoorthy, A.K., 2021. 2D-titanium carbide (MXene) based selective electrochemical sensor for simultaneous detection of ascorbic acid, dopamine and uric acid. J. Mater. Sci. Technol. 72, 122–131.
Naguib, M., Kurtoglu, M., Presser, V., Lu, J., Niu, J., Heon, M., Hultman, L., Gogotsi, Y., Barsoum, M.W., 2011. Two-dimensional nanocrystals produced by exfoliation of Ti3AlC2. Adv. Mater. 23, 4248–4253.
Naguib, M., Come, J., Dyatkin, B., Presser, V., Taberna, P.-L., Simon, P., Barsoum, M.W., Gogotsi, Y., 2012. MXene: a promising transition metal carbide anode for lithium-ion batteries. Electrochem. Commun. 16, 61–64.
Nayak, P., Jiang, Q., Mohanraman, R., Anjum, D., Hedhili, M.N., Alshareef, H.N., 2018. Inherent electrochemistry and charge transfer properties of few-layered two-dimensional Ti 3 C 2 T x MXene. Nanoscale 10, 17030–17037.
Neampet, S., Ruecha, N., Qin, J., Wonsawat, W., Chailapakul, O., Rodthongkum, N., 2019. A nanocomposite prepared from platinum particles, polyaniline and a Ti3C2 MXene for amperometric sensing of hydrogen peroxide and lactate. Mikrochim. Acta 186, 752.
Olsen, E.D., 1986. Analytical chemistry, fourth edition (Christian, Gary D.). J. Chem. Educ. 63, A277.
Palanisamy, S., Lee, H.F., Chen, S.-M., Thirumalraj, B., 2015. An electrochemical facile fabrication of platinum nanoparticle decorated reduced graphene oxide; application for enhanced electrochemical sensing of H 2 O 2. RSC Adv. 5, 105567–105573.
Park, M.-H., Reátegui, E., Li, W., Tessier, S.N., Wong, K.H.K., Jensen, A.E., Thapar, V., Ting, D., Toner, M., Stott, S.L., 2017. Enhanced isolation and release of circulating tumor cells using nanoparticle binding and ligand exchange in a microfluidic chip. J. Am. Chem. Soc. 139, 2741–2749.
Parse, H.B., Patil, I., Ingavale, S., Manohar, C., Roy, V.A.L., Kakade, B., 2019. Efficient oxygen electroreduction kinetics by titanium carbide@ nitrogen doped carbon nanocomposite. Int. J. Hydrogen Energy 44, 23649–23657.
Ramaraj, S., Sakthivel, M., Chen, S.-M., Lou, B.-S., Ho, K.-C., 2019. Defect and additional active sites on the basal plane of manganese-doped molybdenum diselenide for effective enzyme immobilization: in vitro and in vivo real-time analyses of hydrogen peroxide sensing. ACS Appl. Mater. Interfaces 11, 7862–7871.
Rufus, A., Sreeju, N., Philip, D., 2016. Synthesis of biogenic hematite (α-Fe 2 O 3) nanoparticles for antibacterial and nanofluid applications. RSC Adv. 6, 94206–94217.
Ruiyi, L., Tinling, P., Hongxia, C., Jinsong, S., Zaijun, L., 2020. Electrochemical detection of cancer cells in human blood using folic acid and glutamic acid-functionalized graphene quantum dot-palladium@gold as redox probe with excellent electrocatalytic activity and target recognition. Sensor. Actuator. B Chem. 309, 127709.
Seh, Z.W., Fredrickson, K.D., Anasori, B., Kibsgaard, J., Strickler, A.L., Lukatskaya, M.R., Gogotsi, Y., Jaramillo, T.F., Vojvodic, A., 2016. Two-dimensional molybdenum carbide (MXene) as an efficient electrocatalyst for hydrogen evolution. ACS Energy Lett 1, 589–594.
Shamkhalichenar, H., Choi, J.-W., 2020. Non-enzymatic hydrogen peroxide electrochemical sensors based on reduced graphene oxide. J. Electrochem. Soc. 167, 37531.
Silva, R.A.B., Montes, R.H.O., Richter, E.M., Munoz, R.A.A., 2012. Rapid and selective determination of hydrogen peroxide residues in milk by batch injection analysis with amperometric detection. Food Chem. 133, 200–204.
Tavakkoli, H., Akhond, M., Ghorbankhani, G.A., Absalan, G., 2020. Electrochemical sensing of hydrogen peroxide using a glassy carbon electrode modified with multiwalled carbon nanotubes and zein nanoparticle composites: application to HepG2 cancer cell detection. Microchim. Acta. 187, 1–12.
Tehrani, F., Bavarian, B., 2016. Facile and scalable disposable sensor based on laser engraved graphene for electrochemical detection of glucose. Sci. Rep. 6, 1–10.
Teodoro, K.B.R., Migliorini, F.L., Christinelli, W.A., Correa, D.S., 2019. Detection of hydrogen peroxide (H2O2) using a colorimetric sensor based on cellulose nanowhiskers and silver nanoparticles. Carbohydr. Polym. 212, 235–241.
Testa-Anta, M., Ramos-Docampo, M.A., Comesaña-Hermo, M., Rivas-Murias, B., Salgueiriño, V., 2019. Raman spectroscopy to unravel the magnetic properties of iron oxide nanocrystals for bio-related applications. Nanoscale Adv 1, 2086–2103.
Torres, C.R.G., Crastechini, E., Feitosa, F.A., Pucci, C.R., Borges, A.B., 2014. Influence of pH on the effectiveness of hydrogen peroxide whitening. Operat. Dent. 39, E261–E268.
Townsend, T.K., Sabio, E.M., Browning, N.D., Osterloh, F.E., 2011. Photocatalytic water oxidation with suspended alpha-Fe 2 O 3 particles-effects of nanoscaling. Energy Environ. Sci. 4, 4270–4275.
Tripathi, V.S., Kandimalla, V.B., Ju, H., 2006. Amperometric biosensor for hydrogen peroxide based on ferrocene-bovine serum albumin and multiwall carbon nanotube modified ormosil composite. Biosens. Bioelectron. 21, 1529–1535.
Uma, K., Chong, S., Mohan, S.C., Jothivenkatachalam, K., Yang, T.C.-K., Lin, J.-H., 2020. Multi-functional RGO-supported α-Fe2O3 nanocomposites for high-performance pseudocapacitors and visible light–driven photocatalytic applications. Ionics 26, 3491–3500.
V Klassen, N., Marchington, D., McGowan, H.C.E., 1994. H2O2 determination by the I3-method and by KMnO4 titration. Anal. Chem. 66, 2921–2925.
Wang, F., Yang, C., Duan, M., Tang, Y., Zhu, J., 2015a. TiO2 nanoparticle modified organ-like Ti3C2 MXene nanocomposite encapsulating hemoglobin for a mediator-free biosensor with excellent performances. Biosens. Bioelectron. 74, 1022–1028.
Wang, J., Gao, M., Pan, H., Liu, Y., Zhang, Z., Li, J., Su, Q., Du, G., Zhu, M., Ouyang, L., Shang, C., Guo, Z., 2015b. Mesoporous Fe2O3 flakes of high aspect ratio encased within thin carbon skeleton for superior lithium-ion battery anodes. J. Mater. Chem. A. 3, 14178–14187.
Wang, R., Du, X., Wu, Y., Zhai, J., Xie, X., 2018. Graphene quantum dots integrated in ionophore-based fluorescent nanosensors for Na+ and K+. ACS Sens. 3, 2408–2414.

Wang, J., Yang, B., Gao, F., Song, P., Li, L., Zhang, Y., Lu, C., Goh, M.C., Du, Y., 2019. Ultra-stable electrochemical sensor for detection of caffeic acid based on platinum and nickel jagged-like nanowires. Nanoscale Res. Lett. 14, 11.
Xie, X., Chen, C., Zhang, N., Tang, Z.-R., Jiang, J., Xu, Y.-J., 2019. Microstructure and surface control of MXene films for water purification. Nat. Sustain. 2, 856–862.
Yan, C., Wang, J., Lee, P.S., 2015. Stretchable graphene thermistor with tunable thermal index. ACS Nano 9, 2130–2137.
Yang, C., Tang, Y., Tian, Y., Luo, Y., Faraz Ud Din, M., Yin, X., Que, W., 2018. Flexible nitrogen-doped 2D titanium carbides (MXene) films constructed by an ex situ solvothermal method with extraordinary volumetric capacitance. Adv. Energy Mater. 8, 1802087.
Yu, X., Gong, Y., Xiong, W., Li, M., Zhao, J., Che, Y., 2019. Turn-on fluorescent detection of hydrogen peroxide and triacetone triperoxide via enhancing interfacial interactions of a blended system. Anal. Chem. 91, 6967–6970.
Zhang, L., Ni, Y., Wang, X., Zhao, G., 2010. Direct electrocatalytic oxidation of nitric oxide and reduction of hydrogen peroxide based on α-Fe2O3 nanoparticles-chitosan composite. Talanta 82, 196–201.
Zhang, H., Li, M., Cao, J., Tang, Q., Kang, P., Zhu, C., Ma, M., 2018. 2D a-Fe2O3 doped Ti3C2 MXene composite with enhanced visible light photocatalytic activity for degradation of Rhodamine B. Ceram. Int. 44, 19958–19962.
Zheng, W., Zheng, Y.F., Jin, K.W., Wang, N., 2008. Direct electrochemistry and electrocatalysis of hemoglobin immobilized in TiO2 nanotube films. Talanta 74, 1414–1419.
Zou, R., Quan, H., Pan, M., Zhou, S., Chen, D., Luo, X., 2018. Self-assembled MXene (Ti3C2Tx)/α-Fe2O3 nanocomposite as negative electrode material for supercapacitors. Electrochim. Acta 292, 31–38.